



## RESEARCH ARTICLE

10.1029/2022JD036599

### Key Points:

- The super-droplet method, developed for cloud microphysics, is applied to simulate the formation and evolution of nuclear fallout
- The fallout microphysics model predicts that median particle diameter is roughly proportional to square root of integral system mass over yield
- The underlying fallout formation rates and turbulent cloud conditions need to be studied further to improve model predictions

### Correspondence to:

D. L. McGuffin and D. D. Lucas,  
[dana.lynn.mcguiffin@gmail.com](mailto:dana.lynn.mcguiffin@gmail.com);  
[ddlucas@alum.mit.edu](mailto:ddlucas@alum.mit.edu)

### Citation:

McGuffin, D. L., Lucas, D. D., Morris, J. P., Spriggs, G. D., & Knight, K. B. (2022). Super-droplet method to simulate Lagrangian microphysics of nuclear fallout in a homogeneous cloud. *Journal of Geophysical Research: Atmospheres*, 127, e2022JD036599. <https://doi.org/10.1029/2022JD036599>

Received 29 MAR 2022

Accepted 29 AUG 2022

# Super-Droplet Method to Simulate Lagrangian Microphysics of Nuclear Fallout in a Homogeneous Cloud

D. L. McGuffin<sup>1</sup> , D. D. Lucas<sup>1</sup> , J. P. Morris<sup>1</sup> , G. D. Spriggs<sup>1</sup>, and K. B. Knight<sup>1</sup> 
<sup>1</sup>Lawrence Livermore National Laboratory, Livermore, CA, USA

**Abstract** Nuclear detonations produce hazardous local and global particles or fallout. Predicting fallout size, chemical components, and location is necessary to inform officials and determine immediate guidance for the public. However, existing nuclear detonation fallout models prescribe the particle size distributions based on limited observations. In this work, we apply the super-droplet method, which is a numerical modeling technique developed for cloud microphysics, to simulate size distributions of particles in a mushroom cloud formed post-detonation of a nuclear device. We model fallout formation and evolution with homogeneous nucleation and condensation of a single species and a Monte Carlo coagulation algorithm. We verify the numerical methods representing coagulation and condensation processes against analytical test problems. Additionally, we explore several scenarios for the integral system mass and yield in equivalent kilotons (kt) of TNT (trinitrotoluene). The fallout size distribution median diameter  $d_{pg}$  follows a scaling law based on the integral system mass  $m_{v0}$  kg and yield  $Y$  kt:  $d_{pg} = 0.647 m_{v0}^{0.609} / Y^{0.436}$  nm. We test the effect of cloud turbulence, enhanced nucleation and growth, and vapor volatility with a sensitivity study. The range in median diameter predictions for simulations of historical tests performed over the Pacific encompass the measurements of particles sampled from the cloud caps. Predicted median particle size ranges up to 217, 123, 86, and 35 nm for historical tests with yields of 0.2, 0.7, 2, and 10 Mt, respectively. This work can be expanded in many different directions to build a more predictive model for fallout formation.

**Plain Language Summary** Nuclear detonations can result in devastating effects on the surrounding area. In the aftermath, a cloud forms containing radioactive materials formed post-detonation. These radioactive particles can fall out and deposit locally or globally depending on their size. It is important to accurately predict the amount of fallout and fallout particulate size distributions to know the extent and degree of hazard from associated radioactivity. This work applies a technique developed over the last decade for cloud precipitation modeling to the formation and evolution of fallout in mushroom clouds. The numerical techniques implemented to simulate particle growth were verified. Next, we calculated the particle sizes formed under several different nuclear detonation scenarios, varying the integral system mass and the detonation magnitude (energy output). Additionally, we perturbed the underlying assumptions on the rates of particle growth and formation as well as the volatility of the vapourized materials. The range in particle size predicted across these perturbed scenarios encompasses the observed size from atmospheric nuclear tests and prior theoretical estimates.

## 1. Introduction

Nuclear detonations produce rising, hot clouds that quickly cool, forming radionuclide-laden debris in the form of particles (“fallout”) that fall or deposit over the course of seconds to months depending on their size, detonation height, and atmospheric processes. The review of fallout properties by Crocker et al. (1965) determines that high-altitude airbursts generate particles generally smaller than 20  $\mu\text{m}$  in diameter, and observations show there is an inverse relationship between particle size and explosive energy of the device. Nathans et al. (1970) determined analytical estimates of the particle size distribution generated from airbursts and analyzed samples collected from the cloud cap, where the mean particle diameter measured is between 0.1 and 0.3  $\mu\text{m}$ . Their theoretical analysis is limited by their assumption that coagulation and condensation are decoupled, which allows for the application of a similarity transformation. Baker (1987) found nuclear cloud debris is best described with a bimodal lognormal particle number size distribution with median diameters of 0.2 and 0.4  $\mu\text{m}$  for debris formed by vapourized and unmelted/partially melted material, respectively. Recently, Sreekanth et al. (2020) simulated the particle formation and evolution from a high explosive material with a bin-sectional model and found that the mean particle diameter is near 0.01  $\mu\text{m}$  for a 10 kg (or  $10^{-5}$  kt) explosive. High explosive detonations are generally not directly comparable to nuclear detonations due to the different materials and scales of explosive energy.

© 2022 The Authors.

This is an open access article under the terms of the Creative Commons Attribution-NonCommercial License, which permits use, distribution and reproduction in any medium, provided the original work is properly cited and is not used for commercial purposes.



**Figure 1.** Frames from the Hardtack II Wrangell test where the evolution of the cloud is shown at 1.2, 3.5, 15.3, and 26.2 s post-detonation from left to right. We extracted the frames from a video processed by the Film Scanning and Reanalysis Project at Lawrence Livermore National Laboratory and publicly released to YouTube [https://www.youtube.com/watch?v=n3JTutDtq\\_E](https://www.youtube.com/watch?v=n3JTutDtq_E).

Prediction of fallout size, chemical constituents, and spatial distribution is necessary to provide accurate guidance to responders or the public regarding the hazard and environmental impacts of fallout deposition. A nuclear airburst detonation forms a fireball that quickly cools and rises to form a mushroom cloud containing bomb vapor and debris. The Hardtack II Wrangell test was an airburst in 1958 (U.S. Department of Energy, 2015), and four frames of the airburst are shown in Figure 1. The debris is formed and evolved by particle microphysics: nucleation, condensation, and coagulation. As the fireball cools, the vapor becomes supersaturated, nucleating new particles. Then, the nucleated particles grow via condensation of available vapor and coagulation between preexisting particles.

Current post-detonation nuclear fallout models prescribe particle size distributions for the cloud sections empirically, which are based on measurements across limited conditions pertaining to tests conducted primarily in Nevada (Freiling, 1963). Therefore, a motivation of this work is to provide a predictive source term based on a first-principles microphysics algorithm dependent on a wide range of environmental conditions for a large-scale atmospheric dispersion model. Current models, such as the Defense Land Fallout Information Code and K-Division Fallout Code, prescribe an empirical particle size distribution (Bridgman & Bigelow, 1982; Harvey et al., 1992). Modeling the underlying particle microphysics will enable a predictive model for diverse environments like urban or nonarid locations, differing water vapor and oxygen concentrations, and atmospheric states. Incorporating this information would provide better estimates for long-range fallout concentration or dose rates.

Effective prediction of these quantities is vital to protecting the public in these scenarios, so this work presents a computationally efficient way to model particle microphysics in a hot, turbulent cloud. The “super-droplet method” (SDM) developed by Shima et al. (2009) is a computationally efficient way to simulate cloud microphysics from first principles (Grabowski et al., 2019; Morrison et al., 2020; Shima et al., 2020). SDM represents the particle size distribution by sampling it with a set of computational particles called “super-droplets.” Each super-droplet represents several real particles with similar characteristics or attributes. They are created through particle nucleation and their sizes are adjusted as condensation and coagulation evolve. In the Lagrangian framework, each super-droplet acts as a computational particle with fallout-specific attributes (size, composition, and shape) in addition to the typical Lagrangian attributes of particle position, velocity, and mass. This paper presents, to our knowledge, the first application of SDM to simulate particle microphysical processes of fallout in cooling fireball clouds. Previously, SDM has been utilized to model several applications, including ice nucleation, mixed/ice phase clouds, cloud microphysics simulating precipitation, marine fog, and cloud chemistry (Arabas & Shima, 2013; Brdar & Seifert, 2018; Dziekan et al., 2019; Grabowski, 2020; Jaruga & Pawlowska, 2018; Richter et al., 2021; Seifert et al., 2019; Shima et al., 2020, etc.).

In this work, we aim to improve current post-detonation fallout models by developing a module that simulates the fallout size distribution in a nuclear airburst. This tool would provide a predictive capability under diverse environments and conditions based on first principles. The fireball contains the vapourized device and any entrained environmental material. We utilize iron oxide (FeO) as a proxy for the species of the vapourized integral system mass since the properties of FeO have been studied across a range of conditions and prior modeling work assumed the vapourized material is FeO (Nathans et al., 1970). Additionally, previous work investigating temperatures relevant to post-detonation conditions experimentally observed FeO (Koroglu et al., 2018, 2022).

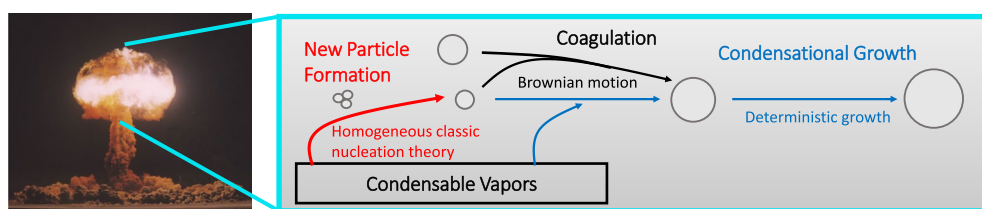


**Figure 2.** Objective of this work is to simulate fallout formation and evolution within a homogeneous fireball and early cloud with the underlying particle microphysical processes: nucleation, condensation, and coagulation.

We simulate the fallout formation within a homogeneous fireball composed of air and FeO. Although the reality is that the fireball has a more complex composition and spatial distribution, our assumptions provide a good test case for developing the fallout SDM.

## 2. Fallout Super-Droplet Method

In this work, we simulate particle microphysics inside a cooling fireball generated from an airburst with a time evolving zero-dimensional model that does not resolve any spatial dimensions, as shown in Figure 2. This zero-dimensional model is significantly limited in representing a real nuclear airburst due to the assumption of a well-mixed, homogeneous mushroom cloud, which can encompass on the order of  $1 \text{ km}^3$  depending on the test magnitude. The aim of this work is to illustrate the potential of the SDM in modeling nuclear fallout microphysics, so we test the numerical technique in a zero-dimensional setup that can be extended to a spatially resolving model in future work. High-altitude detonations, like the airbursts considered here, do not include complexities such as ground interactions so that the post-detonation cloud is spherical, symmetric, well-mixed (Gowardhan et al., 2021), and modeling a homogeneous cloud in zero-dimensions is justified.

We specify the temperature and volume of the system as described in Section 2.1. The particles are formed and their evolution is based on the underlying microphysical processes described in Section 2.2. These dynamics are numerically tracked with super-droplets described in Section 2.2.1. The processes considered here are nucleation, condensation, and coagulation occurring within seconds to minutes post-detonation. Thus, we do not consider water vapor or delayed ambient cloud microphysics in this work, but coupling to a water cloud microphysics routine is a possible area for future work. We do not include the entrainment of any surrounding particles like dust, soil, or sea spray since we are focused on isolated airbursts, but other materials could be included without difficulty assuming an appropriate entrainment model is established. Since airbursts result in submicron particle sizes with very small gravitational settling velocities, we do not include the deposition of particles (e.g., a  $100 \text{ nm}$  particle settles at  $2.4 \text{ cm hr}^{-1}$  at  $2000 \text{ K}$ ). Thus, the predicted particle size distributions are representative of a nuclear airburst in the absence of precipitation and gravitational settling, but wet and dry deposition should be considered in future work. Additionally, the formation of cloud droplets from fallout in clouds is not considered here since we are not modeling water vapor, but this is another direction for future work. The model variables and parameters are listed in Tables A1 and A2 in the Appendix.

### 2.1. Fireball and Cloud Conditions

Temperature and volume are very important conditions in our predictions as they strongly affect the concentration of vapor available and its partial pressure. Here, we describe the assumed temperature and cloud volume curves, which we apply as boundary conditions. Both of these variables are dependent on the test magnitude specified by the system yield,  $Y$ . The system yield is measured by the equivalent quantity (kt) of TNT that would produce the same amount of energy when it explodes;  $1 \text{ kt}$  of TNT produces  $4.184 \cdot 10^{12} \text{ J}$  energy (Glasstone & Dolan, 1977). Estimates of the fireball temperature and subsequent cooling are from thermal radiation measurements taken during the 1950 and 1960s nuclear tests. Hillendahl's equation is an empirical relationship for temperature  $T(t)$  degrees Kelvin at time  $t$  seconds based on the system yield  $Y$  kt (Freiling et al., 1965).

$$T(t) = 2.26 \cdot 10^3 Y^{0.1} t^{-0.335} \quad (1)$$

Several of the films capturing the historical nuclear tests have been digitized and analyzed as part of the Film Scanning and Reanalysis Project at Lawrence Livermore National Laboratory (Spriggs et al., 2020). This film

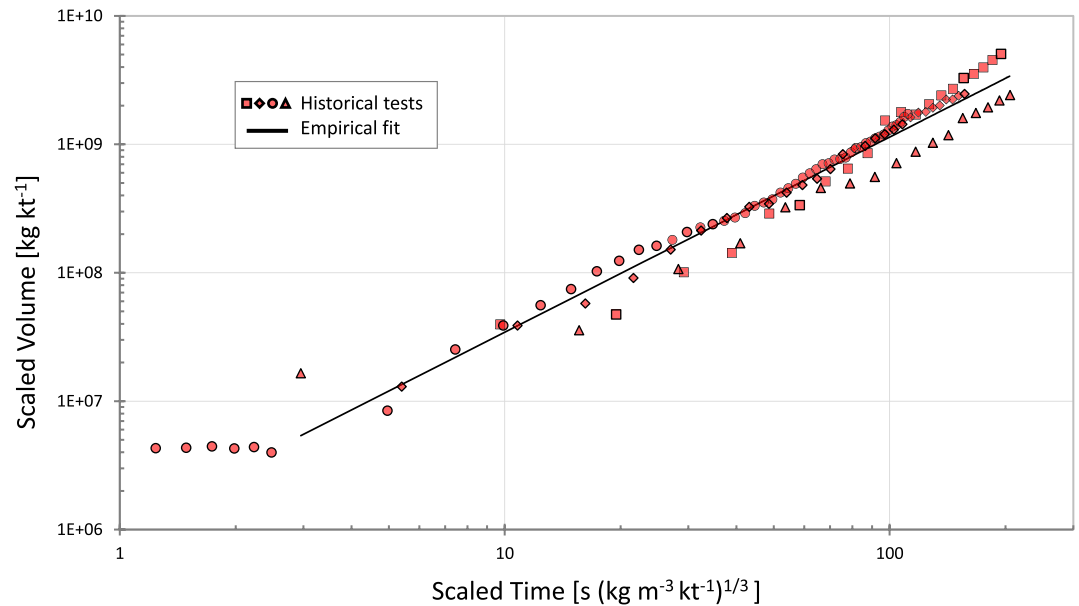


**Figure 3.** Cloud volume measured from historical films and the fitted expansion curve are given in red markers and a black line, respectively. The different test events are shown in different marker shapes. The scaled volume and scaled time are based on the scaling laws.

analysis uncovered scaling laws for post-detonation cloud size, which show self-similarity. Cloud sizes of different yields and characteristics have the same behavior, that is, they are self-similar, when their scaling law is applied. The scaled cloud volume  $V_s$   $\text{kg kt}^{-1}$  and scaled time  $t_s$   $\text{s kg}^{1/3} \text{m}^{-1} \text{kt}^{-1/3}$  are based the air density  $\rho_0$   $\text{kg m}^{-3}$  at the height of burst and test yield  $Y$   $\text{kt}$ .

$$V_s = V \rho_0 / Y \quad (2)$$

$$t_s = t(\rho_0 / Y)^{1/3} \quad (3)$$

Spriggs et al. (2020) estimated the cloud volume versus time from films. This data is in scaled units from four separate tests is shown in Figure 3. We fit a logarithmic expansion curve to the self-similar cloud volume data to determine the cloud volume  $V(t)$   $\text{m}^3$  at time  $t$   $\text{s}$ .

$$\ln V_s(t_s) = 1.5198 \ln t_s + 13.854 \quad (4)$$

We assume an air density of  $1.02 \text{ kg m}^{-3}$  corresponding to a  $1.85 \text{ km}$  height of burst with the U.S. Standard Atmosphere (Seinfeld & Pandis, 2006) in all model results presented here. This empirical expansion curve is valid for  $t_s > 3 \text{ s kg}^{1/3} \text{m}^{-1} \text{kt}^{-1/3}$ , as shown in Figure 3. If the scaled time is below this limit, we assume a minimum volume defined using the asymptotic fireball radius  $R_{\text{asym}}$   $\text{m}$  (Spriggs et al., 2020).  $R_{\text{asym}}$  corresponds to the maximum fireball radius before the mushroom cloud forms (Glasstone & Dolan, 1977).

$$R_{\text{asym}} = 67.4(Y / \rho_0)^{1/3} \quad (5)$$

## 2.2. Particle Microphysics

The microphysical processes defining the fallout properties are modeled with the population balance partial differential equations on the particle size distribution  $n(v, t)$  for particle volume  $v$  at time  $t$  (Seinfeld & Pandis, 2006).

$$\begin{aligned} N_i(t) &= \int_0^\infty n(v, t) dv \\ \frac{\partial n(v, t)}{\partial t} &= J_{\text{nuc}}(t) \delta(v - v_{\text{nuc}}) + \frac{1}{2} \int_0^v K(v - q, q) n(v - q, t) n(q, t) dq \\ &\quad - n(v, t) \int_0^\infty K(v, q) n(q, t) dq - \frac{\partial}{\partial v} [I(v) n(v, t)] \end{aligned} \quad (6)$$

$N_t$  is the total number concentration of particles. Nucleation is the source of tiny particles with size  $v_{nuc}$  based on the nucleation cluster size (see Equation 9). The generation of new particles is modeled with a delta function across particle size based on the nucleation rate  $J_{nuc}$ . The particles are grown by both coagulation and condensation.  $K(v, q)$  is the coagulation kernel for the collision of particles with size  $v$  and  $q$ . Coagulation is both a source and sink of particles with size  $v$  due to smaller particles colliding and creating particles of size  $v$  and particles of size  $v$  are scavenged by larger particles, respectively. The growth of particles due to condensation is modeled with the last term in Equation 6 based on the condensation rate  $I(v)$  to particle size  $v$ . Condensation is negative since it is analogous to an advection term across particle size: it is a source term of  $n(v, t)$  as gas condenses to smaller particles and it is a sink of  $n(v, t)$  as vapor grows particles of size  $v$  to larger sizes.

This integro-differential equation can be integrated by discretizing  $n(v, t)$  by particle size, which is often utilized in atmospheric models as a sectional or bin approach. However, the sectional technique is not computationally efficient for this application since it tracks every section of the size distribution even if there are no particles in a bin. Fallout deposition processes are often easier to track in a Lagrangian reference frame, so modeling microphysics in an already existing Lagrangian framework is more computationally efficient than adding an Eulerian grid for sectional microphysics. Additionally, the sectional approach is prone to numerical diffusion across particle size when modeling the contribution from condensation (Chandrakar et al., 2022; Grabowski et al., 2019). Instead, we approach the problem from a Lagrangian reference frame and utilize the SDM to solve the population balance. Shima et al. (2009) estimate that SDM incurs less computational cost than a sectional method when modeling more than 2–4 attributes.

The SDM determines how each process individually affects the particle size distribution in terms of the number concentration and particle size. During a master time step  $\Delta t$  of 0.1 s, the three microphysical processes are modeled with individual time steps based on the numerical technique used to model each process: nucleation, coagulation, and condensation. In this work, we assume a well-mixed control volume, so no spatial discretization is required, resulting in a zero-dimensional model.

### 2.2.1. Super-Droplet Definition

The SDM utilized here is based on work by Shima et al. (2009) where a super-droplet is defined as a numerical Lagrangian particle with attributes describing the fallout properties. Since we are only simulating one species at a time, the population of modeled fallout is described with just two time-varying state variables.  $\xi_i(t)$  and  $r_i(t)$  represent the multiplicity and radius of the  $i$ th super-droplet at time  $t$ , respectively. Simulating multicomponent particles is accomplished by adding an attribute for the mass of each species. The number concentration  $N$  of particles with size  $v_i$  represented by a super-droplet is calculated by normalizing  $\xi_i(t)$  with the cloud volume  $V(t)$ .

$$N(v_i, t) = \xi_i(t)/V(t) \quad (7)$$

The evolution of all  $N_s$  super-droplets based on  $\xi_i(t)$  and  $r_i(t)$  is described by particle nucleation, coagulation, and condensation in the following Sections 2.2.2, 2.2.3, and 2.2.4, respectively.

### 2.2.2. New Particle Formation

As the cloud cools, it becomes supersaturated with the vapourized materials, which we assume is iron oxide. The saturation ratio ( $S$ ) of a compound is defined as the partial vapor pressure divided by its saturation vapor pressure over a flat liquid surface ( $p_{sat}$ ).

$$p_{sat}(t) = \exp \left\{ \frac{H_v}{R} (T_{boil}^{-1} - T(t)^{-1}) \right\} \quad (8)$$

$H_v$  is the enthalpy of vapourization,  $R$  is the universal gas constant, and  $T_{boil}$  is the boiling point. Classic nucleation theory describes the formation rate of new particles from vapor ( $J_{nuc}$  #s<sup>-1</sup>) due to homogeneous nucleation based on the capillary approximation. The free energy of nucleation is determined based on the decrease due to the new, stable phase and the increase due to the surface tension of the new phase (Farley, 1952). The radius of nucleated clusters ( $r_{nuc}$  m) is calculated from the maximum free energy of formation and  $J_{nuc}$  is determined from a Boltzmann distribution for the number of clusters formed.

$$\begin{aligned} r_{nuc} &= \frac{2\sigma v_a}{k_B T(t) \ln S} \\ J_{nuc} &= \frac{p_{sat} m_v(t) N_{av}}{\rho T(t) m} \sqrt{\frac{2\sigma m}{\pi R k_B}} \exp \left\{ \frac{-4\pi \sigma r_{nuc}^2}{3 k_B T(t)} \right\} \end{aligned} \quad (9)$$

$\sigma$  is the cluster surface tension,  $\rho$  is the cluster mass density,  $v_a$  is the atomic volume,  $m$  is the molar mass,  $N_{av}$  is Avogadro's number,  $k_B$  is the Boltzmann constant, and  $m_v$  is the mass of vapor.  $N_{nuc}$  new super-droplets are added with a radius of  $r_{nuc}$  and multiplicity  $\xi_{nuc}$  if the multiplicity is at least one.

$$\xi_{nuc} = J_{nuc} \Delta t_{nuc} / N_{nuc} \quad (10)$$

We randomly choose to apply the ceiling or floor to determine  $\xi_{nuc}$  in the above equation to mitigate rounding errors.

Currently, the mechanism and rate of atmospheric particle nucleation are an open area of research (Adams et al., 2013). Although classical nucleation theory is known to underestimate particle formation rates for many applications, it provides a valuable reference point for evaluating particle formation processes for cooling fireballs. We expect other nucleation mechanisms, such as heterogeneous nucleation or multicomponent nucleation, to play an important role.

The nucleation time step is 0.1 s to match the overall model time step. The vapor mass is decreased based on the particle mass nucleated, as shown in the following expression.

$$m_v(t) = m_v(t - \Delta t_{nuc}) - \frac{4}{3} \pi r_{nuc}^3 \rho \xi_{nuc} \quad (11)$$

The top panel of Figure 7 shows the cloud temperature and the FeO saturation ratio to illustrate classical nucleation theory for a cooling fireball. Utilizing this method for FeO vapor in an 10 kt airburst with 20 super-droplets for  $N_{nuc}$ , homogeneous nucleation begins 13 s post-detonation in this test case.

The simulation of fallout begins once 20 particles ( $N_{nuc}$ ) are nucleated at a saturation ratio significantly greater than 1, as shown in an example for a 10 kt yield and 1,500 kg  $m_{v0}$  scenario in Figure 7a. Initializing the fallout population with 20 super-droplets allows the coagulation algorithm to be applied immediately. Then, nucleation continues to create super-droplets at each model time step  $\Delta t$  of 0.1 s if the cloud is still supersaturated. In each nucleation event subsequent to the initial formation event, only one super-droplet is created ( $N_{nuc} = 1$ ) to prevent the number of super-droplets from increasing drastically over time. To additionally avoid increasing the number of super-droplets too much, the new super-droplet is combined with the smallest super-droplet  $k$  if the following conditions are met where the volume  $V(t)$  is determined from the cloud expansion curve.

$$|r_k - r_{nuc}| \leq 1.2 r_k \quad (12)$$

$$\xi_k / V(t) \leq 10 \text{ cm}^{-3} \quad (13)$$

The technique for combining the nucleated and preexisting super-droplets is described in the merging algorithm in Section 2.3.

### 2.2.3. Coagulation

Coagulation occurs as two particles' Brownian motion causes them to collide, resulting in one particle with their combined volume. While the total particle volume is conserved, the total number of particles decreases as particles collide. The probability of two particles with radius  $r_i$  and  $r_j$  colliding is based on their coagulation kernel  $K(r_i, r_j)$ . However, since the SDM does not directly simulate each particle, we apply an "all or nothing" method of coagulation between super-droplets (Unterstrasser et al., 2017). Here, we assume that coagulation of two super-droplets translates to a number of one-on-one collisions based on the minimum multiplicity ( $\min\{\xi_i, \xi_j\}$ ) between the two super-droplets. The algorithm is described in detail by Shima et al. (2009), but we summarize it below.

In the SDM algorithm, coagulation is simulated as a Monte Carlo method with the probability of  $\alpha^{\text{th}}$ -pair of super-droplets colliding  $P_\alpha$  based on their coagulation kernel  $K(r_{\alpha_1}, r_{\alpha_2})$ . The coagulation kernel is based on the Brownian motion of the two particles from their diffusion coefficients  $D_i$ .



$$K(r_i, r_j) = 4\pi(D_i + D_j)(r_i + r_j)\beta_{ij} \quad (14)$$

$$D_i = \frac{k_B T(t)}{6\pi\mu r_i} \left( \frac{5 + 4\lambda/r_i + 6\lambda^2/r_i^2 + 18\lambda^3/r_i^3}{5 - \lambda/r_i + (8 + \pi)\lambda^2/r_i^2} \right) \quad (15)$$

The kernel is determined at a temperature  $T(t)$ , air viscosity  $\mu$ , mean free path  $\lambda$ , and the Fuchs noncontinuum correction factor  $\beta_{ij}$  (Fuchs, 1964).

Instead of evaluating the probability of coagulation for every unique pair of super-droplets, the algorithm chooses a randomized list of unique pairs to evaluate at each coagulation time step. This reduces the computational expense from  $\mathcal{O}(N_s^2)$  to  $\mathcal{O}(N_s)$  based on the number of super-droplets  $N_s$ . The collision probability of the  $\alpha^{th}$  pair (super-droplets  $\alpha_1, \alpha_2$ ) from the randomized list is  $P_\alpha$ .

$$P_\alpha = K(r_{\alpha_1}, r_{\alpha_2}) \frac{\xi_{\alpha_1} N_s (N_s - 1) \Delta t_{coag}}{2V_{coag} \lfloor N_s/2 \rfloor} \quad (16)$$

Here  $\alpha_1$  is defined by  $\xi_{\alpha_1} \geq \xi_{\alpha_2}$ ,  $\Delta t_{coag}$  is the time step for coagulation, and  $V_{coag}$  is the volume of the coagulation cell. In the zero-dimensional model described in this paper, the coagulation cell is the size of the cloud  $V(t)$  and  $\Delta t_{coag} = 0.01$  s. When the coagulation cell is well-mixed, the coagulation algorithm exactly simulates stochastic Brownian coagulation. Deviations from the well-mixed case were investigated for cloud microphysics by Dziekan and Pawlowska (2017), finding that large coagulation cells overestimate the rate of collisions. This should be investigated for mushroom clouds in future work toward developing a nuclear fallout model with spatial variations.

The coagulation time step should be chosen so that  $P_\alpha \leq 1$  for a given  $V_{coag}$ . However, if this condition is not satisfied, the algorithm simulates the coagulation of more than two particles colliding (based on  $\bar{\gamma}_\alpha$  defined below).  $\bar{\gamma}_\alpha$  is the number of  $\alpha_1$  particles scavenged by an  $\alpha_2$  particle, which is stochastic based on the uniformly sampled random number  $\phi$ .

$$\gamma_\alpha = \begin{cases} \lfloor P_\alpha \rfloor + 1 & \text{if } \phi < P_\alpha - \lfloor P_\alpha \rfloor \\ \lfloor P_\alpha \rfloor & \text{otherwise} \end{cases} \quad (17)$$

$$\bar{\gamma}_\alpha = \min \left\{ \gamma_\alpha, \left\lfloor \frac{\xi_{\alpha_1}}{\xi_{\alpha_2}} \right\rfloor \right\} \quad (18)$$

If  $\gamma_\alpha$  is nonzero, there is a collision event between the  $\alpha^{th}$  pair of super-droplets with  $\bar{\gamma}_\alpha$  particles from super-droplet  $\alpha_1$  colliding with one particle represented by  $\alpha_2$ . Thus, the multiplicity of  $\alpha_1$  is decreased to account for the scavenging by  $\alpha_2$  and the  $\alpha_2$  radius is increased based on the volume of particles colliding.

$$\begin{aligned} \xi_{\alpha_1} &\mapsto \xi_{\alpha_1} - \bar{\gamma}_\alpha \xi_{\alpha_2} \\ r_{\alpha_2} &\mapsto (\bar{\gamma}_\alpha r_{\alpha_1}^3 + r_{\alpha_2}^3)^{1/3} \end{aligned} \quad (19)$$

If a super-droplet is completely scavenged during coagulation, then the scavenging super-droplet is split in two. If a super-droplet multiplicity reaches zero, the super-droplet is deleted from the list (step 5 of the algorithm in Shima et al., 2009).

#### 2.2.4. Condensation

As the fireball cools, particles also grow from the condensation of vapor. Not only does the vapor need to be supersaturated like in nucleation, but the energy barrier due to the Kelvin effect must not be too large. The Kelvin effect energy barrier is due to surface tension forces from the curvature of a particle. The saturation pressure over a curved droplet with radius  $r_i$  is  $p_{d,i}$  assuming the droplet temperature is the same as its surroundings.

$$p_{d,i}(t) = p_{sat} \exp \left\{ \frac{2\sigma m}{R\rho T(t)r_i(t)} \right\} \quad (20)$$

As vapor condenses, it releases energy by heating up the droplet, which is less than 0.001 K for a 10 kt yield and 1,500 kg integral system mass, so we consider it as negligible at these extreme conditions. The super-droplet radius after condensation is determined by integrating the ordinary differential equation for radius-squared.

$$\frac{dr_i^2}{dt} = \frac{D_v m}{2\rho RT(t)} Nu_M(r_i) [p_\infty(t) - p_{d,i}(t)] \quad (21)$$

$D_v$  is the diffusivity of FeO in air,  $p_\infty(t)$  is the partial vapor pressure of FeO at time  $t$  based on the vapor mass  $m_v(t)$ , and  $Nu_M$  is the Nusselt number for mass transport to correct for the transition regime.

$$Nu_M = \frac{2Nu}{2 + Nu} \quad (22)$$

$$Nu = \frac{2r_i RT_{melt}}{D_v m (p_d(t) - p_\infty(t))} \left( \frac{p_d(t) m^{1/2}}{\sqrt{2\pi RT(t)}} - \frac{p_\infty(t) m_{air}^{1/2}}{\sqrt{2\pi RT(t)}} \right)$$

$T_{melt}$  is the melting point of FeO and  $m_{air}$  is the molecular weight of air.

Since both  $Nu_M$  and  $p_d$  depend on the droplet radius, we integrate Equation 21 with an implicit Euler solver using the Newton-Raphson method with a maximum of 25 iterations. Convergence is determined if the fractional change in radius is less than  $10^{-10}$ . The time step for condensation is  $\Delta t_{cond} = 0.01$  s. The vapor mass is reduced based on the amount condensed.

$$m_v(t) = m_v(t - \Delta t_{cond}) - \frac{4}{3} \pi \rho \sum_{i=1}^{N_s} \xi_i (r_i^3(t) - r_i^3(t - \Delta t_{cond})) \quad (23)$$

### 2.3. Merging Super-Droplets

Since the nucleation routine creates new super-droplets to model particle nucleation, the number of super-droplets increases as nucleation persists in a simulation. This significantly increases the computation time, so we implemented a “merging” algorithm to limit  $N_s$  to  $N_{max}$  similar to that used by Unterstrasser and Sölch (2014). If the number of super-droplets exceeds the specified threshold ( $N_{max} = 100$ ), we find the two super-droplets ( $j, k$ ) with the closest radius and determine if they should be merged.

$$\frac{|r_j - r_k|}{\min(r_j, r_k)} \leq 0.05 \quad (24)$$

If the above condition is met, the two super-droplets are combined by conserving particle volume as described below and super-droplet  $k$  is deleted.

$$\begin{aligned} \xi_j &\mapsto \xi_j + \xi_k \\ r_j &\mapsto \left( \left( 1 - \frac{\xi_k}{\xi_j + \xi_k} \right) r_j^3 + \frac{\xi_k}{\xi_j + \xi_k} r_k^3 \right)^{1/3} \end{aligned} \quad (25)$$

## 3. Results and Discussion

In this section, we discuss and analyze results from the super-droplet fallout model described above. First, the numerical methods are verified with different test cases in Section 3.1. Next, we investigate the model predictions for specific airbursts in Section 3.2. Finally, we compare the model predictions to measurements from historical tests performed over the Pacific Ocean in Section 3.3.

### 3.1. SDM Numerical Tests

The coagulation and condensation routines require numerical methods to model particle growth, while nucleation is an instantaneous formation of new particles and is easily represented numerically as a pulse of new super-droplets. Therefore, we performed a verification test for the coagulation algorithm and a numerical test for the condensation solver using simple test problems with analytical solutions.



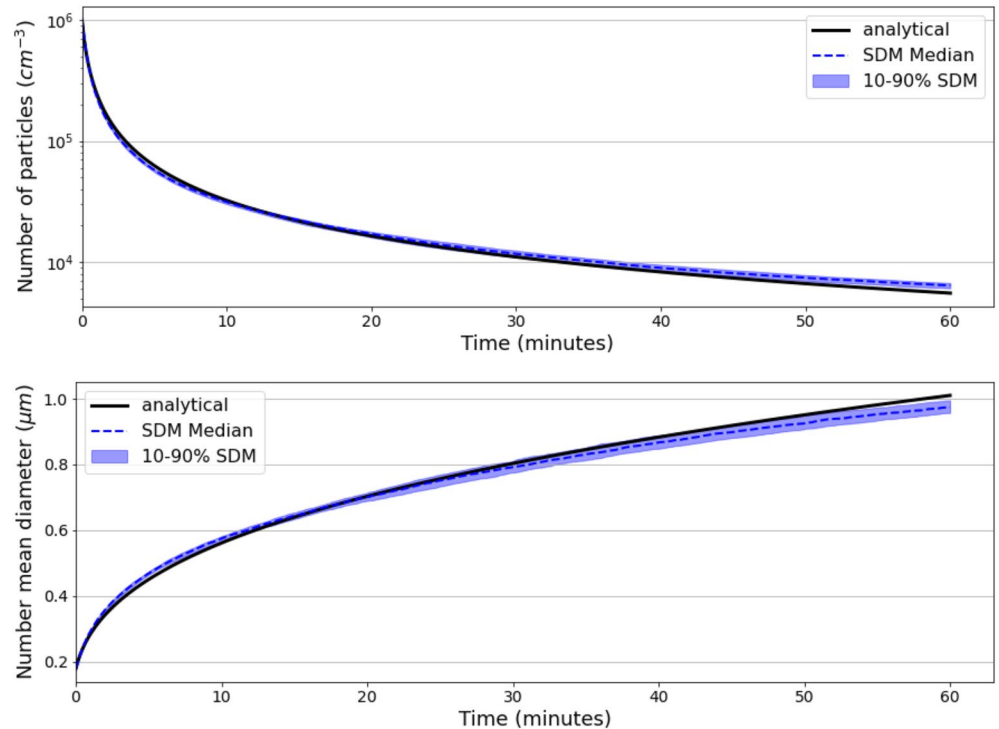


**Figure 4.** Validation of the super-droplet method coagulation routine with a test problem. Statistics for the ensemble of super-droplet method (SDM) simulations are shown along with the analytical solution for the number concentration and number mean diameter over time in the top and bottom figures, respectively. The shaded region shows the 10–90th percentiles and the blue dashed line shows the 50th percentile among the ensemble of 50 SDM simulations.

### 3.1.1. Coagulation

Particle coagulation with a coagulation kernel  $K$  consistent across particle sizes and an initial exponential particle size distribution has an analytical solution for the size distribution evolution (Seinfeld & Pandis, 2006). The particle number size distribution  $n(v, t)$  for a particle volume  $v$  at time  $t$  is

$$n(v, t) = \frac{N_0^2}{V_0(1 + t/\tau)^2} \exp \left\{ -v \frac{N_0}{V_0(1 + t/\tau)} \right\} \quad (26)$$

where  $N_0$  and  $V_0$  are the initial number and volume concentrations, respectively, and  $\tau$  is the timescale for coagulation with a coagulation kernel  $K = 2/(\tau N_0)$ . The resulting total number concentration and number mean diameter of particles with  $N_0 = 10^6 \text{ cm}^{-3}$ ,  $V_0 = 4,189 \text{ } \mu\text{m}^3 \text{ cm}^{-3}$ , and  $\tau = 20 \text{ s}$  is used to test the Monte Carlo coagulation algorithm in the fallout SDM. The diameter is calculated assuming spherical particles.

The Monte Carlo coagulation scheme described in Section 2.2.3 is stochastic, so we ran the coagulation algorithm over an ensemble of 50 scenarios with an initial exponential size distribution and a coagulation kernel described above. The SDM coagulation routine predicts the number concentration and diameter associated with the 1,000 super-droplets as they grow over one hour. Figure 4 shows the total number concentration and the number mean diameter (mean diameter of super-droplets weighted by their number concentrations) in the top and bottom panels, respectively. The shaded region and dashed blue line show the 10–90 percentile range and the 50th percentile across the ensemble of simulations. The median predictions at the final time have errors of 16% and 3.5% from the analytical solution for the number concentration and number mean diameter, respectively.

Using more super-droplets would improve the accuracy of the coagulation algorithm with a penalty of computational cost. We modeled the coagulation test problem above, varying the number of super-droplets to investigate the error rate. Figure 5 shows that increasing the number of super-droplets significantly decreases the magnitude of predicted error relative to the analytical solution. More than 200 super-droplets are needed to achieve an error of 30% and 8% in total number concentration and number mean diameter, respectively. Additionally, the

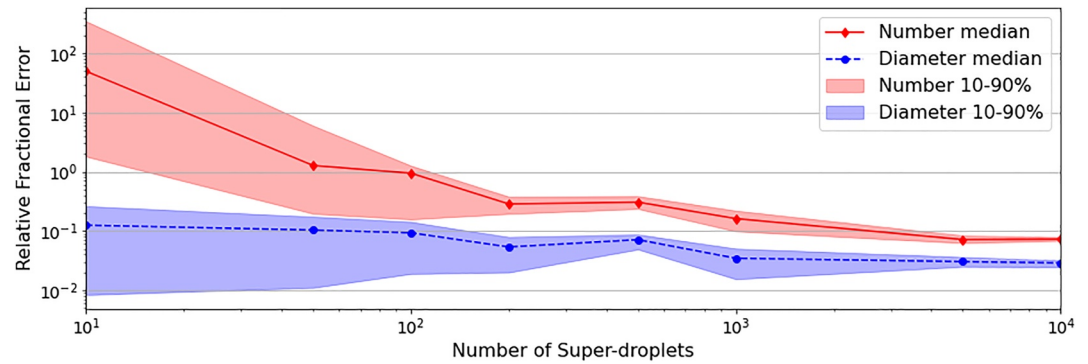


**Figure 5.** Super-droplet method coagulation performance at the end of a 1 hr simulation when varying the number of super-droplets. The absolute value of the average relative error in the predicted number concentration and number mean diameter is shown in the red diamonds and blue circles, respectively. The red and blue-shaded areas show the range between the 10th and 90th percentiles for the number concentration and number mean diameter, respectively.

variability between different scenarios decreases as more super-droplets are used, which is shown by the decreasing area of the shaded regions with the number of super-droplets. The total number concentration is predicted less accurately than the mean diameter metric since the zeroth moment is generally more susceptible to under-sampling than any higher moments like the mean diameter. The mean or median diameter is used as the metric to evaluate the predicted size distribution in the nuclear post-detonation simulations presented in the remainder of this work, so we focus on the mean diameter error. As described in Section 2.3, up to 100 super-droplets are used in the simulations of airbursts shown in Sections 3.2 and 3.3. This value balances the trade-off between accuracy and computational efficiency since the verification tests here show the predicted mean diameter is within 10% error with 100 super-droplets.

### 3.1.2. Condensation

An analytical solution to the differential Equation 21 for condensational growth is found if the Kelvin effect is negligible so that  $p_d = p_{\text{sat}}$  and if we assume the continuum regime ( $Nu_M = 2$ ). The solution to the condensation equation for particle diameter  $d_i(t)$  at time  $t$  is.

$$d_i^2(t) = d_{i0}^2 + 8 \frac{D_v m}{\rho RT} [p_{\infty} - p_{\text{sat}}] t \quad (27)$$

for an initial particle diameter  $d_{i0}$  at time 0 (Seinfeld & Pandis, 2006). We used this equation to simulate the growth of three particles with  $d_{i0}$  0.01, 0.1, and 1  $\mu\text{m}$  at 298 K with  $p_{\infty} - p_{\text{sat}} = 10^{-9}$  atm. The growth of the three particles from numerical integration compared to the analytical particle diameter is shown in Figure 6. The Newton-Raphson method results in zero error, so we confirm that the condensation numerical routine accurately integrates the condensational growth rate.

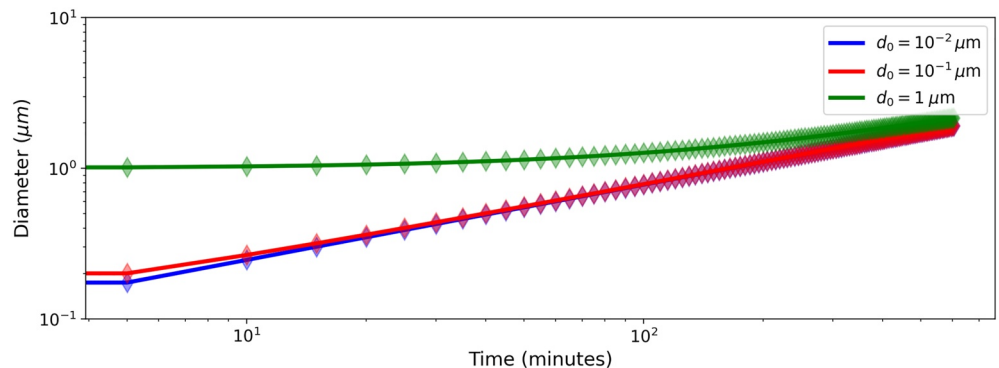


**Figure 6.** Validation of the super-droplet method condensation routine with a test problem. The analytical and predicted particle diameter for three initial sizes are shown in the solid lines and diamond markers, respectively.

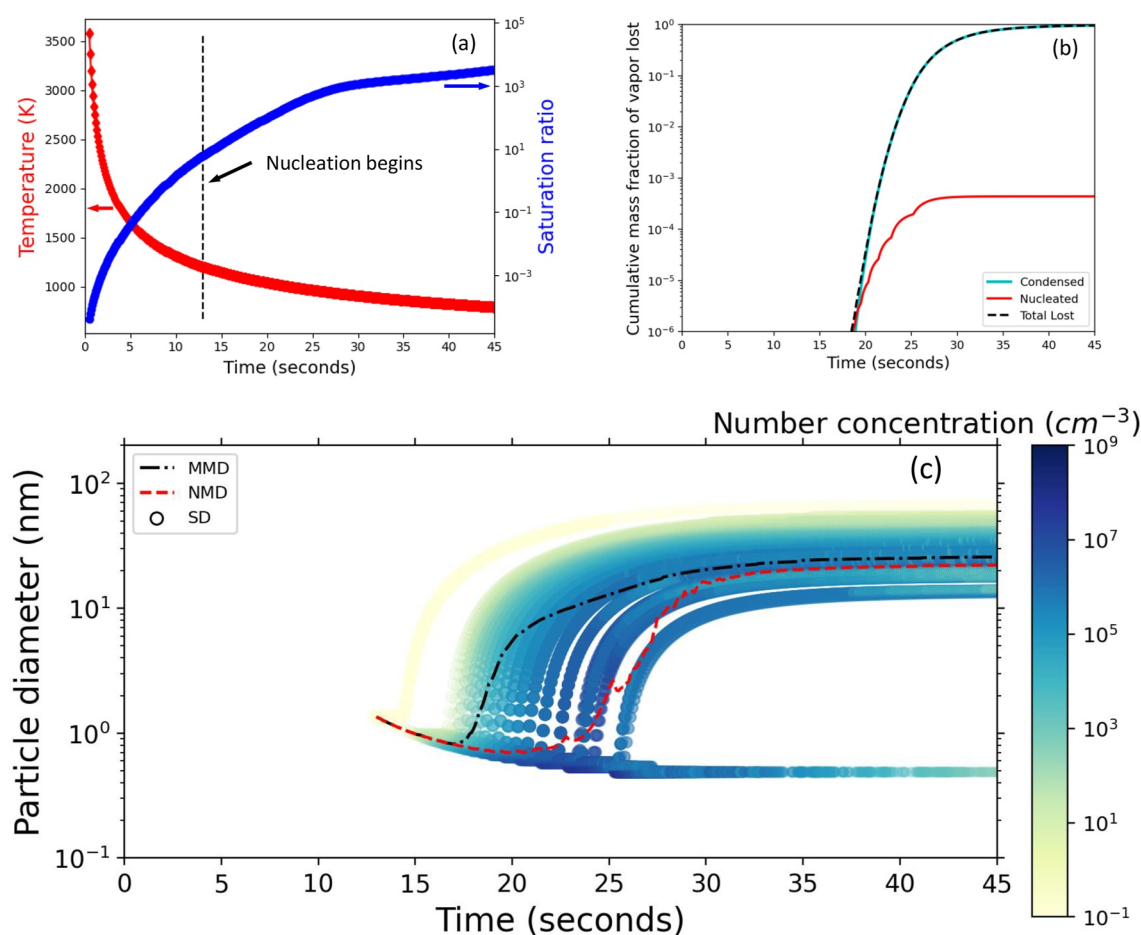


**Figure 7.** Time series showing the particle evolution and the homogeneous fireball conditions. The top left panel (a) shows the cloud's cooling curve and saturation ratio in the red left and blue right y-axes, respectively. The top right panel (b) shows the cumulative fraction of vapor lost due to condensation and nucleation. The bottom panel (c) shows the super-droplet size evolution with the number concentration on the color map and the number mean diameter and mass-mean diameter shown in the red and black dashed curves, respectively.

### 3.2. Airburst Simulations

Combining all components of the model described in Section 2, we simulate an airburst scenario with a 10 kt yield and 1,500 kg integral system mass. The cloud cooling and vapor saturation ratio curves are shown in Figure 7a. The fireball cooling increases the saturation ratio, while the cloud expansion and depletion of vapor to form and grow particles decreases the saturation ratio. In this case, the effect of temperature dominates as the saturation ratio increases even though 99.7% of the vapor is depleted (shown in Figure 7b). Utilizing the relevant temperature and volume profiles for an 10 kt yield event, the predicted particle size distribution evolution is shown in Figure 7c. The scatter plot shows the size of each super-droplet at each time step with color from the multiplicity normalized by the cloud volume. A transparency scale is applied that logarithmically increases as the number concentration decreases, which smooths noise in the visualization due to coagulation.

First, particles near 1 nm are nucleated at 13 s and a few particles are grown with condensation, shown with a light yellow curve. As the supersaturation increases, the critical cluster radius decreases, so that the nucleated particles decrease in size. In turn, the Kelvin effect increases so that condensation is not favorable until the cloud cools enough for the vapor pressure to exceed the droplet saturation pressure. As particles are grown and nucleation continues, the probability of coagulation increases, so that the smallest particles are scavenged by the larger particles. The combination of these effects results in a number mean diameter profile that decreases and then increases and stabilizes near 20 nm. The number mean diameter is sensitive to coagulation, which is stochastic, so the number mean diameter time series includes this noise as opposed to the mass mean diameter in Figure 7c.

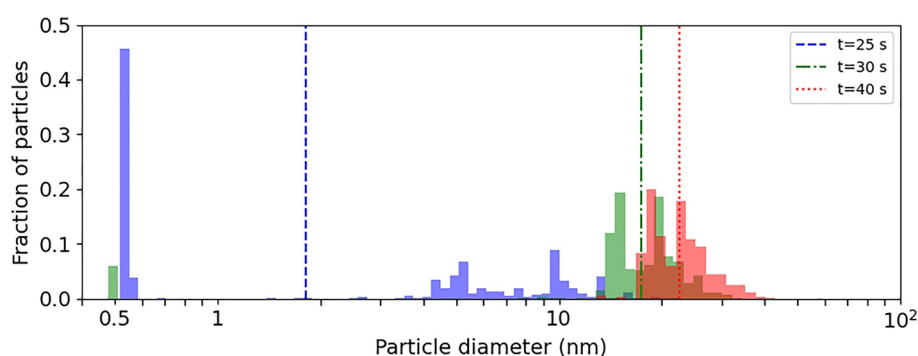


**Figure 8.** Super-droplets representing the particle size distribution at 25, 30, and 40 s during the simulation using an empirical, logarithmic expansion curve in the blue, green, and red histograms, respectively. The dashed, dash-dotted, and dotted lines show the median diameter of the 25, 30, and 40 s particle population, respectively, in the color corresponding to the histogram.

As the particle size distribution evolves, both the number mean diameter and the width increase. This is shown in Figure 8 with the predicted median diameter and particle size distribution at 25, 30, and 40 s in the blue, green, and red histograms, respectively. These histograms are generated by combining 10 ensembles of the same scenario. Each simulation uses a maximum of 100 super-droplets, so the histograms are sampling the size distribution with 1,000 super-droplets.

None of the histograms pictured match a lognormal distribution well. The histograms at 25, 30, and 40 s are all multimodal with a decreasing nucleation mode as time progresses. The multimodal behavior is present in each ensemble member (not shown here).

The other nuclear detonation microphysics model from Nathans et al. (1970) predicts similarly small particle sizes with a median diameter of 55 nm, which is less than a factor of three different from the 20 nm diameter predicted here. The comparison of our predictions to measurements is investigated in the following Section 3.3.

### 3.2.1. Variations of Particle Size to Airburst Properties

The main inputs to the fallout SDM are integral system mass and yield ( $m_{v0}$ ,  $Y$ ), which determine the cloud size, cooling rate, and vapor partial pressure. We performed a series of simulations, varying these inputs for airburst conditions, to determine how the particle size distribution changes. As the yield increases, the temperature and size of the cloud increase. As the integral system mass increases, the vapor has a larger saturation ratio. At the highest yield and lowest system mass, the saturation ratio is very small since it takes longer to cool and by that time the cloud has expanded significantly to dilute the vapor. On the other hand, there is a larger driving force for condensation and nucleation at the lowest yield and largest system mass.

We performed a total of 450 simulations with mass and yield inputs chosen randomly from four Latin hypercubes (McKay et al., 1979), which evenly samples the desired input space. Combinations of high yield and low mass result in a dilute cloud in which the homogeneous nucleation rate is reduced even though the vapor is supersaturated. Therefore, we limit our analysis to cases with yields below 300 kt and masses above 10 kg as shown in Figure 9. We sampled the input space in four studies that avoided the extreme corner of low mass and high yield, and numbers three and four added more resolution

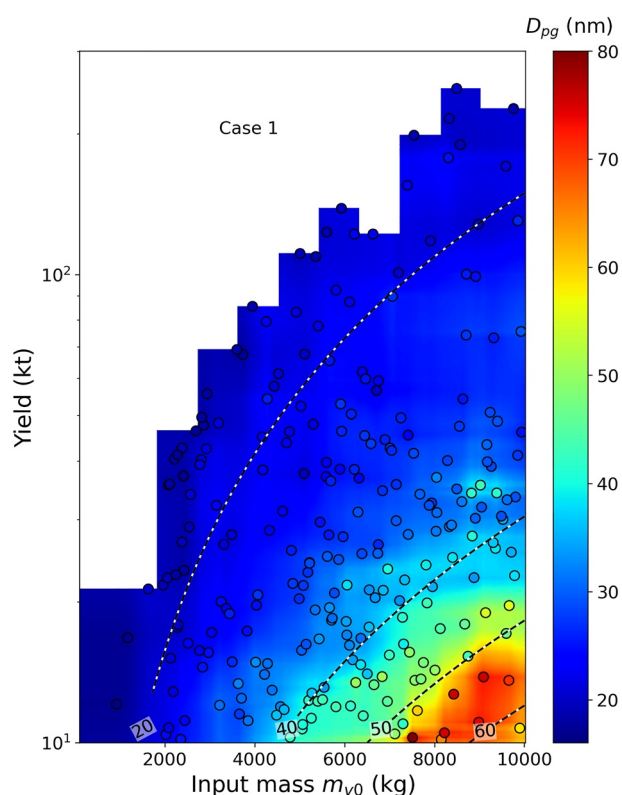


**Figure 9.** Variations of predicted median particle diameter to integral system mass and yield. The circles show the predictions from the fallout super-droplet method, and the background color shows an interpolation with a random forest regression. Contour lines for the fitted scaling law for integral system mass and yield.

**Table 1**  
*Latin Hypercubes Sampled for the Mass, Yield, and Particle Size Analysis*

Study No.	Number of simulations	Mass ( $m_{v0}$ ) range (kg)	Yield (Y) range (kt)
1	50	10–1,000	10–1,000
2	100	1,000–10,000	10–10,000
3	200	2,000–10,000	10–500
4	100	5,000–10,000	10–50

in the high mass and low yield corner. The sampling ranges for the four Latin hypercubes are listed in Table 1.

Despite limiting the sampling input space to avoid limitations in homogeneous nucleation, several anomalous simulations occurred in which less than 99% of the vapor was lost after 40 min post-detonation. We consider these simulations as “non-depleted” since the vapor is not depleted after cooling past its melting point. These were cases with roughly a ratio of  $m_{v0}/Y < 50 \text{ kg kt}^{-1}$ . These results are excluded since they are most likely cases where the homogeneous nucleation scheme breaks down. The predicted median diameters of the remaining fallout distributions at the final simulated time are shown in Figure 9 as the circles. The background color is interpolated from

the simulation values using a random forest fit with 500 trees, a maximum depth of 10, and no more than two features. White contour lines are shown for the equation  $Am_{v0}^b/Y^c$  with coefficients  $A = 0.647$ ,  $b = 0.609$ ,  $c = 0.436$  fitted from the model predictions.

As described above, the low yield and high mass section, or high  $m_{v0}/Y$ , has a larger driving force for condensation and nucleation earlier in the cloud evolution. This results in larger particles with a median diameter near 60 nm for  $m_{v0}/Y = 900 \text{ kg kt}^{-1}$  compared to particles smaller than 20 nm for  $m_{v0}/Y = 50 \text{ kg kt}^{-1}$ . The results show that, under the assumptions considered here, the median diameter of fallout approximately scales with  $\sqrt{m_{v0}/Y}$ . Prior work by Nathans et al. (1970) show a similar trend with  $m_{v0}/Y$  from their analytical estimate of the median fallout diameter for Brownian motion coagulation:  $8.5(m_{v0}/Y^{0.69})^{1/3}$ . The larger coefficient and smaller exponents lead to a stronger dependence to yield at low integral system mass. The estimated particle sizes from the Nathans et al. (1970) expression are approximately a factor of two larger than our fallout SDM predictions. These differences are reasonable considering our different approaches. Nathans et al. (1970) used an exponential cooling curve with an empirical relationship for the temperature of initial particle formation with respect to the yield, had a factor of five lower surface tension, and assumed the particle size distribution is self-preserving. In fact, a factor of two discrepancy among model predictions is common and acceptable for aerosol modeling and nucleation predictions, respectively (e.g., Chen et al., 2019; Jung et al., 2010; Semeniuk & Dastoor, 2018; Westervelt et al., 2013).

### 3.3. Sensitivity Comparison With High-Yield Observations

Available observations of the number particle size distribution were sampled 2–3 hr post-detonation from the cap of high yield airbursts performed under operation Dominic. Given the delay between fallout formation and collection, the observations could be impacted by cloud processing. The particles were collected on filter paper mounted on an aircraft wing, and the size was measured with an electron microscope after processing the filters. In the experimental analysis discussion, Nathans et al. (1970) note an experimental lower and upper bound in the measured size distributions, which is approximately from 20 to 420 nm for the cap observations shown here. Therefore, the measured median diameter is likely biased high since particles smaller than 20 nm may not have been detected. Table 2 shows the yield for each of the historical tests (Nathans et al., 1970). In the fallout SDM,

we input the yield of each scenario and assume an integral system mass of 3,200 kg to compare with prior estimates by Nathans et al. (1970).

The mass and yield of these tests correspond to the model input space ( $m_{v0}/Y < 50 \text{ kg kt}^{-1}$ ) where the model predicts vapor available past its melting point (nondepleted) due to the limitations of the homogeneous nucleation scheme. This is due to running the fallout super-droplet model with incorrect nucleation, condensation, or coagulation rates. To compare the model with measurements, we performed sensitivity studies varying several of the uncertain parameters and process rates. Uncertainties in the model include (a) volatility or speciation, (b) nucleation mechanism, and (c) enhancement in coagulation probability due to in-cloud turbulence. To test these three uncertainties, we performed 18 simulations varying two species volatilities, three coagulation rates (nominal, medium, and high), and three condensation

**Table 2**  
*Operation Dominic Nuclear Tests With Particle Size Distribution Measurements Sampled From the Cap*

Case number <sup>a</sup>	Yield (kt)
1	200
2	700
3	2,000
4	10,000

<sup>a</sup>Cases 1, 2, 3, and 4 correspond to E, F, G, and H in Nathans et al. (1970), respectively.



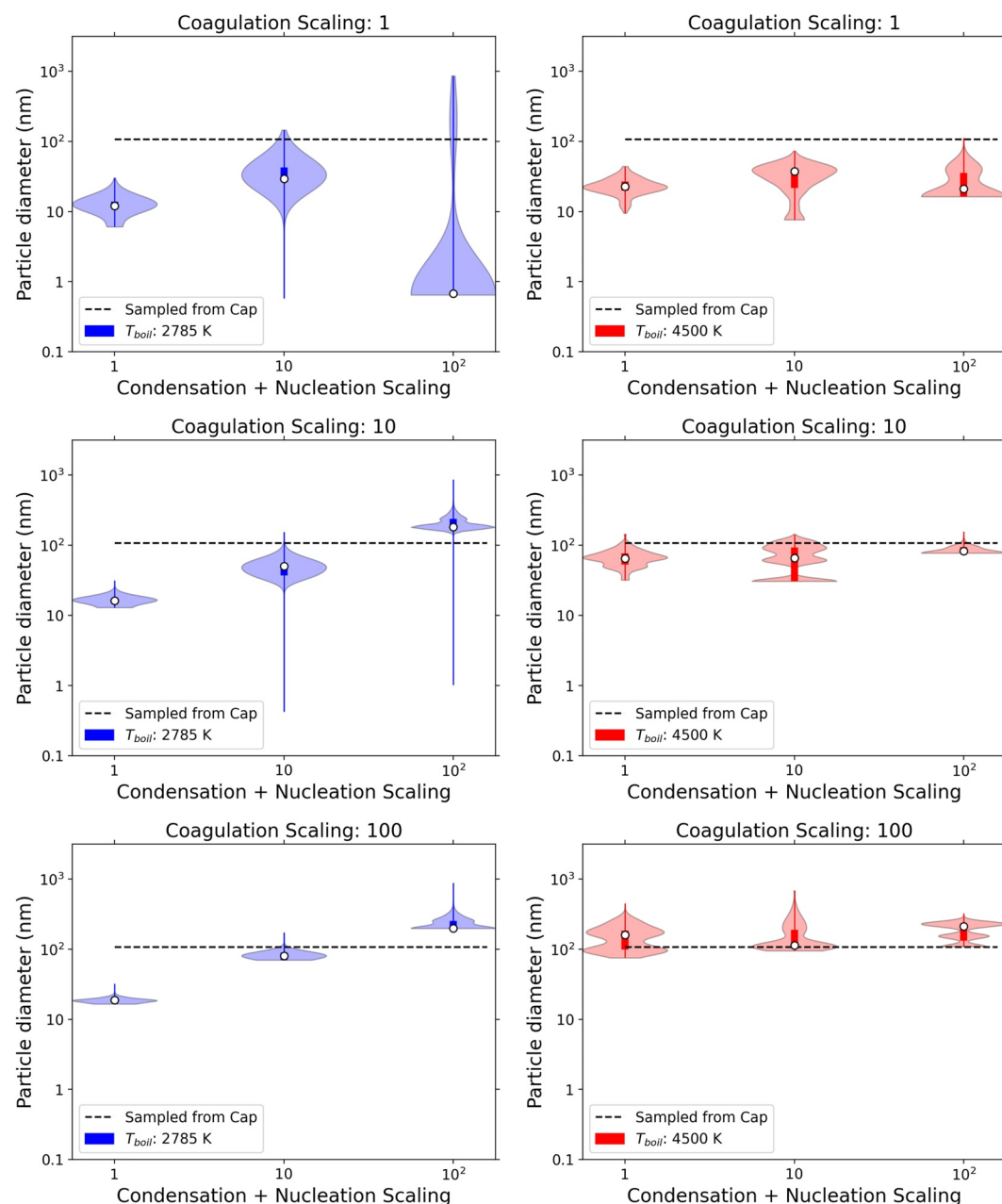


**Figure 10.** Violin plots of predicted particle size distribution from varying species volatility, coagulation kernel, and rate of condensation and nucleation compared with the observed median diameter in the dashed line for Case 1 ( $Y = 200$  kt and  $m_{00} = 3,200$  kg). The median diameter is shown as a white circle, the interquartile range is shown in the thick lines, and the range is shown in the thin vertical lines. Each plot shows the distribution of predicted particle diameters from the super-droplets for a range of scaling factors applied to both the condensation and nucleation rates. The left column shows predictions for iron oxide and the right column represents a species with a higher boiling point (SrO). The top, middle, and bottom rows show predictions from scaling the coagulation kernels by a factor of 1, 10, and 100, respectively.

and nucleation rates (nominal, medium, and high). The “volatile” species considered is FeO with a boiling point of 2785 K while the species used to represent refractory compounds is SrO with a boiling point of 4500 K. Microphysical uncertainties are tested by varying two scaling factors at nominal, medium, and high values of 1, 10, and 100: one applied to both condensation growth rate and nucleation rate, and one applied to the coagulation kernels. Varying these scaling factors helps to understand the effects of preferential clustering of particles in turbulent eddies and alternative nucleation mechanisms.



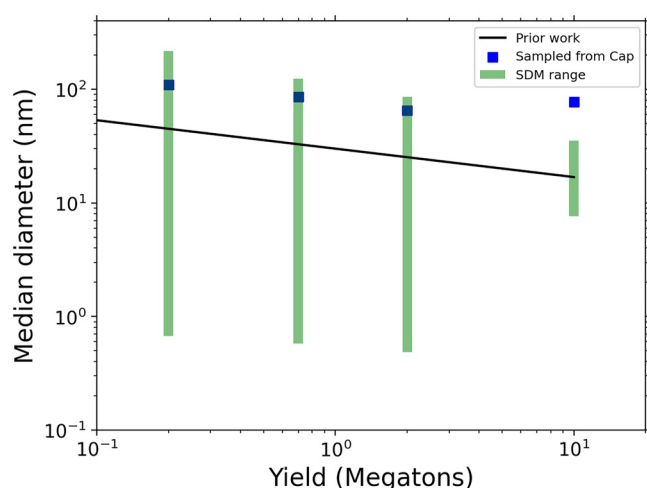


**Figure 11.** Median particle diameter of fallout in cloud cap produced by airburst test shots in the Pacific. Measurements from aircraft samples are shown in blue squares and the prediction from an analytical expression is shown in the black line. The range in predicted median diameter from super-droplet method (SDM) sensitivity studies for the four test shots is shown in the green rectangles.

We performed these sensitivity simulations for Case 1, which assumes  $Y = 200$  kt and  $m_{i,0} = 3,200$  kg. The resulting particle size distribution from each simulation of the test is shown as violin plots in Figure 10. The median diameter, interquartile range, and overall range in the predicted size distributions are shown as white circles, thick lines, and thin lines along with the observed median diameter sampled from the cloud cap in dashed lines (Nathans et al., 1970). The nominal fallout SDM prediction is shown with the blue violin in the top left figure at the condensation and nucleation scaling factors of one, but only 38% of the vapor is depleted. All scenarios except five resulted in fully depleted vapor. The nominal condensation and nucleation rates of FeO resulted in 38%, 18%, and 10% vapor depleted for coagulation kernels scaled by factors of 1, 10, and 100, respectively. Additionally, the nominal condensation and nucleation rates of SrO resulted in 98% and 85% vapor depleted for coagulation kernels scaled by factors of 10 and 100, respectively. In general, the predicted median particle diameter increases as the coagulation scaling factor increases, the boiling point of the compound increases, and the scaling factor on condensation and nucleation rates increases.

This analysis shows there are multiple combinations of the uncertain species and process rates that can match the observations. In general, increases in the probability of coagulation enhance the number of collisions and therefore the particle size. Additionally, vapor compounds with a higher boiling point nucleate particles faster at the early stages of the mushroom cloud formation,

so the particles can grow to a larger size compared to a lower boiling point species. Finally, enhancing the condensation and nucleation rates increase the particle size since the flux of vapor growing the particles increases.

There are a few exceptions to these trends. In the more volatile species with a coagulation scaling factor of 1 (top left plot), the median diameter decreases as the condensation and nucleation scaling factor increases from 10 to 100. Even though the median diameter decreases by an order of magnitude, the maximum particle size increases, resulting in a bimodal size distribution. The more volatile species in blue shown in the left figures are more sensitive to increases in condensation and nucleation rates compared to the more refractory species shown in the right figures. This occurs because the particle size is limited by the amount of vapor available. The refractory species has a higher nominal homogeneous nucleation rate than the volatile species. Thus, the more refractory species is already reaching the limit on the particle growth rate, even with nominal nucleation and condensation rates.

We performed the same set of 18 sensitivity simulations described above for cases 2, 3, and 4. To compare the model to measurements, we identify the subset of simulations that are fully depleted. We calculate the range in median diameter for this subset of simulations in each case described in Table 2. Cases 1, 2, 3, and 4 include 13, 10, 10, and 5 fully depleted scenarios out of the 18 scenarios run for each case, respectively.

Figure 11 shows the range in fallout SDM predictions of median diameter in the green-shaded areas against the yield of each test. The maximum predicted diameter decreases as the yield increases due to the larger and more dilute clouds. The range in predicted size mostly encompasses the observations and prior estimates shown in blue squares and a black line, respectively. Prior work by Nathans et al. (1970) determined an analytical expression for the median diameter based on the mass and yield. The dependency on yield is shown for a constant integral system mass  $m_{i,0} = 3,200$  kg in Figure 11. The range in predicted particle size from the SDM decreases as the yield increases, which is due to fewer fully depleted scenarios. For example, in Case 4 all of the simulations with FeO resulted in nondepleted vapor.

Case 4 with a 10 Mt yield is the only observation that does not fall within the predicted range of median diameter. Model assumptions that could explain this mismatch include: the cloud is assumed to be spatially uniform, fallout is modeled as a single chemical compound, and incorrect cloud cooling and expansion curves are prescribed. These assumptions can be tested by including the fallout SDM in a three-dimensional hydrodynamics model simulating the post-detonation effects. The large sensitivity to perturbing homogeneous nucleation suggests that alternate mechanisms, like heterogeneous or ion-induced nucleation, should also be explored

since different mechanisms may have a nonlinear effect on median particle size. Additionally, particle microphysics should be coupled to a chemical kinetic model for better representation of the vapor species within the mushroom cloud.

#### 4. Conclusions

In this work, we extended the SDM, which has been developed for and used to simulate microphysics in ambient atmospheric clouds. The modeling technique was applied to simulate a different type of cloud formed post-detonation of a nuclear device, a “mushroom cloud.” In this first application, we simplified the problem as a zero-dimensional expanding and cooling volume. The SDM is utilized to track the size and number concentration of fallout formed as the mushroom cloud rises and cools. We modeled fallout formation and evolution with homogeneous nucleation, condensation of a single species, and the probabilistic coagulation algorithm (Shima et al., 2009).

Numerical methods representing coagulation and condensation processes agree well with analytical test problems. Additionally, we simulated several scenarios for the integral system mass in kg and yield in equivalent kt of TNT. Once the vapor is depleted, the fallout median diameter follows a scaling law based on the integral system mass and yield ( $0.647m_{\text{tot}}^{0.609}/Y^{0.436}$ ). This model is limited due to uncertainty in the mechanism of nucleation, and the energy barrier for homogeneous particle formation in dilute clouds ( $m_{\text{v}}/Y < 50 \text{ kg kt}^{-1}$ ) is too high for the vapor to nucleate new particles above their melting point. This needs to be explored further with various nucleation mechanisms and with a higher-dimensional fluid dynamic model that represents the spatially nonuniform vapor concentration field.

Enhanced coagulation rates due to cloud turbulence and enhanced nucleation and growth result in a wide range of median particle diameters. Additionally, this sensitivity of particle size to coagulation, nucleation, and growth rates is dependent on vapor volatility. This result is illustrated by modeling the formation and evolution of SrO, which is more refractory than FeO. The range in predictions for four scenarios simulating historical tests performed over the Pacific encompass three of the four measured median diameters sampled from each test's cloud cap.

This work can be expanded in many different directions to build a more predictive model for the fallout formed from a nuclear detonation. A model with multiple species would provide a better representation of the fallout composition. Ideally, this is accomplished with a coupled chemistry model describing the complex reactions in the fireball and subsequent cloud. The radionuclides should also be modeled with the Bateman equation describing nuclear decay chains. Limitations in the current model results due to homogeneous nucleation rates highlight that the model should include a nucleation mechanism that more accurately describes the particle formation, like heterogeneous and ternary nucleation.

The assumption of spatially uniform mass density and temperature over the cloud allowed this work to develop the model in a zero-dimensional framework but also results in over simplifications. Future work should explore applying the SDM to one-, two-, and three-dimensional systems to reduce errors due to the well-mixed assumption and allow extension to detonations with ground interactions. Eventually, we should couple the microphysics model with a hydrodynamic model (e.g., Morris et al. (2021)) that resolves turbulence and the spatial concentration and temperature fields. Hydrodynamic models, which utilize passive Lagrangian tracers for understanding the flow field, would provide accurate cooling and expansion rates. While these boundary conditions are defined by empirical relationships in this work. Additionally, resolving turbulence would allow the model to include an enhancement to the coagulation kernel accounting for turbulent shear collisions.

This is the first time, to our knowledge, that first principle particle microphysics has been included in a model predicting post-detonation fallout. The fallout SDM described here will allow future models to predict fallout properties and their dispersion computationally efficiently and accurately under diverse environments.

#### Appendix A: Notation for the Variables and Parameters Used in the Model Are Defined in Tables A1 and A2

The Chapman-Enskog equation is used to determine the diffusion coefficient  $D_v$  of vapor in air at atmospheric pressure  $P$  and molecular weight of air  $m_{\text{air}}$  with an average molecular radius  $\sigma$  (Seinfeld & Pandis, 2006).

**Table A1**

Variable Definitions

Symbol	Units	Description
$t$	s	Time since detonation
$V(t)$	$\text{m}^3$	Volume
$T(t)$	K	Temperature
$R_{\text{asym}}$	m	Asymptotic radius of fireball
$n(v, t)$	$\# \text{m}^{-4}$	Particle number size distribution for particle volume $v \text{ m}^3$
$(\xi_i, r_i)$	(#, m)	Super-droplet $i$ attributes describing number of particles and their radius
$K(r_i, r_j)$	$\text{m}^3 \text{s}^{-1}$	Coagulation kernel between particles with radii $r_i$ and $r_j$
$p_{\text{sat}}$	kPa	Saturation pressure of vapor
$r_{\text{nuc}}$	m	Nucleated particle radius
$S$	—	Saturation ratio of nucleating vapor
$m_v$	kg	Vapor mass
$J_{\text{nuc}}$	$\# \text{s}^{-1}$	Nucleation rate of particles
$D_i$	$\text{m}^2 \text{s}^{-1}$	Brownian diffusion coefficient of particle with diameter $d_i$
$\mu$	$\text{kg m}^{-1} \text{s}^{-1}$	Air viscosity
$\lambda$	m	Mean free path of air
$P_\alpha$	—	Probability of the $\alpha^{\text{th}}$ pair of super-droplets colliding
$p_{d,i}$	kPa	Saturation vapor pressure over a droplet surface with diameter $d_i$
$p_\infty$	kPa	Partial pressure of vapor
$Nu$	—	Dimensionless Nusselt number
$\bar{\gamma}_\alpha$	#	Number of particles (from $\alpha_1$ super-droplet) scavenged by a particle from the $\alpha_2$ super-droplet

$$D_v = \frac{3k_B^{1.5} T^{1.5}}{8P\sigma^2 \sqrt{2\pi}} \sqrt{1/m_v + 1/m_{\text{air}}} \quad (\text{A1})$$

**Table A2**

Parameter Definitions With Values for FeO in Parenthesis

Symbol	Units	Description
$m$	$\text{g mol}^{-1}$	Molecular weight of vapor (71.85)
$H_v$	$\text{kJ mol}^{-1}$	Enthalpy of vapourization (230.3)*
$T_{\text{boil}}$	K	Temperature of boiling point (2,785)*
$T_{\text{melt}}$	K	Temperature of melting point (1,647)*
$\rho$	$\text{kg m}^{-3}$	Density of liquid (5,900)*
$\sigma$	$\text{J cm}^{-2}$	Surface tension of liquid $\left(2.1 \cdot 10^{-7} \frac{\text{J}}{\text{m}} (1.5T_{\text{boil}} - T)\right)^\dagger$
$N_{\text{av}}$	$\text{mol}^{-1}$	Avogadro's number ( $6.02 \cdot 10^{23}$ )
$v_a$	$\text{m}^3 \text{mol}^{-1}$	Atomic volume $\left(\frac{m}{N_{\text{av}} \rho}\right)$
$R$	$\text{J mol}^{-1} \text{K}^{-1}$	Universal gas constant (8.314)
$k_B$	$\text{m}^2 \text{kg s}^{-2} \text{K}^{-1}$	Boltzmann constant ( $1.38 \cdot 10^{-23}$ )
$D_v$	$\text{cm}^2 \text{s}^{-1}$	Diffusivity of vapor in air <sup>‡</sup>
$\Delta t_x$	s	Time step of process $x$
$N_s$	—	Total number of super-droplets
$N_{\text{nuc}}$	—	Number of super-droplets initially generated representing nucleated particles
$Y$	kt	Yield of detonation in kt of TNT
$m_{\text{v}0}$	kg	Integral system mass ( $m_v(t=0)$ )

Note. \*Cornell and Schwertmann (2003). <sup>†</sup>The Eötvös equation (Palit, 1956) has been investigated further by Kou et al. (2019), and in this work we assume a similar functional form.

## Data Availability Statement

The fallout super-droplet method code is available online (McGuffin & Lucas, 2022).

## Acknowledgments

This work was performed under the auspices of the U.S. Department of Energy by Lawrence Livermore National Laboratory under Contract DE-AC52-07NA27344 with IM release number LLNL-JRNL-833257. This work was funded by Laboratory Directed Research and Development Strategic Initiative project "Influence of the Environment on Post-Detonation Chemistry and Debris Formation" with tracking code 20-SI-006. We would like to acknowledge Nathan Wimer for valuable discussions and insight.

## References

- Adams, P. J., Donahue, N. M., & Pandis, S. N. (2013). Atmospheric nanoparticles and climate change. *AIChE Journal*, 59(11), 4006–4019. <https://doi.org/10.1002/aic.14242>
- Arabas, S., & Shima, S. (2013). Large-eddy simulations of trade wind cumuli using particle-based microphysics with Monte Carlo coalescence. *Journal of the Atmospheric Sciences*, 70(9), 2768–2777. <https://doi.org/10.1175/JAS-D-12-0295.1>
- Baker, G. H. (1987). *Implications of atmospheric test fallout data for nuclear winter*. Doctoral dissertation, Air Force Institute of Technology. Retrieved from <https://apps.dtic.mil/sti/citations/ADA182607>
- Brdar, S., & Seifert, A. (2018). McSnow: A monte-carlo particle model for riming and aggregation of ice particles in a multidimensional microphysical phase space. *Journal of Advances in Modeling Earth Systems*, 10(1), 187–206. <https://doi.org/10.1002/2017MS001167>
- Bridgman, C., & Bigelow, W. (1982). A new fallout prediction model. *Health Physics*, 43(2), 205–218. <https://doi.org/10.1097/00004032-198208000-00002>
- Chandrakar, K. K., Morrison, H., Grabowski, W. W., & Bryan, G. H. (2022). Comparison of Lagrangian superdroplet and Eulerian double-moment spectral microphysics schemes in large-eddy simulations of an isolated cumulus congestus cloud. *Journal of the Atmospheric Sciences*, 79(7), 1887–1910. <https://doi.org/10.1175/JAS-D-21-0138.1>
- Chen, X., Yang, W., Wang, Z., Li, J., Hu, M., An, J., et al. (2019). Improving new particle formation simulation by coupling a volatility-basis set (VBS) organic aerosol module in NAQPMS+APM. *Atmospheric Environment*, 204, 1–11. <https://doi.org/10.1016/j.atmosenv.2019.01.053>
- Cornell, R. M., & Schwertmann, U. (2003). *The iron oxides: Structure, properties, reactions, occurrences, and uses* (Vol. 2). John Wiley & Sons, Ltd. <https://doi.org/10.1002/3527602097>
- Crocker, G. R., O'Connor, J. D., & Freiling, E. C. (1965). *Physical and radiochemical properties of fallout particles* (Tech. Rep.). Naval Radiological Defense Laboratory. Retrieved from <https://www.osti.gov/servlets/purl/4582648>
- Dziekan, P., & Pawlowska, H. (2017). Stochastic coalescence in Lagrangian cloud microphysics. *Atmospheric Chemistry and Physics*, 17(22), 13509–13520. <https://doi.org/10.5194/acp-17-13509-2017>
- Dziekan, P., Waruszewski, M., & Pawlowska, H. (2019). University of warsaw Lagrangian cloud model (UWLCM) 1.0: A modern large-eddy simulation tool for warm cloud modeling with Lagrangian microphysics. *Geoscientific Model Development*, 12(6), 2587–2606. <https://doi.org/10.5194/gmd-12-2587-2019>
- Farley, F. J. M. (1952). The theory of the condensation of supersaturated ion-free vapour. *Proceedings of the Royal Society of London A*, 212, 530–542. <https://doi.org/10.1098/rspa.1952.0099>
- Freiling, E. C. (1963). *Fractionation. III. Estimation of degree of fractionation and radionuclide partition for nuclear debris* (Tech. Rep.). Naval Radiological Defense Laboratory. Retrieved from <https://apps.dtic.mil/sti/citations/AD0423725>
- Freiling, E. C., Crocker, G. R., & Adams, C. E. (1965). Nuclear debris formation. In *Radioactive fallout from nuclear weapons tests: Proceedings of the second conference* (pp. 1–41). U.S. Atomic Energy Commission. Retrieved from <https://www.osti.gov/biblio/4590875>
- Fuchs, N. A. (1964). In C. N. Davies (Ed.), *The mechanics of aerosols*. Dover Publications, Inc.
- Glasstone, S., & Dolan, P. J. (1977). *The effects of nuclear weapons*. Third edition. Retrieved from <https://www.osti.gov/biblio/6852629>
- Gowardhan, A. A., McGuffin, D. L., Lucas, D. D., Neuscamman, S. J., Alvarez, O., & Glascoe, L. G. (2021). Large eddy simulations of turbulent and buoyant flows in urban and complex terrain areas using the Aeolus model. *Atmosphere*, 12(9), 1107. <https://doi.org/10.3390/atmos12091107>
- Grabowski, W. W. (2020). Comparison of Eulerian bin and Lagrangian particle-based schemes in simulations of pi chamber dynamics and microphysics. *Journal of the Atmospheric Sciences*, 77(3), 1151–1165. <https://doi.org/10.1175/JAS-D-19-0216.1>
- Grabowski, W. W., Morrison, H., Shima, S.-I., Abade, G. C., Dziekan, P., & Pawlowska, H. (2019). Modeling of cloud microphysics: Can we do better? *Bulletin of the American Meteorological Society*, 100(4), 655–672. <https://doi.org/10.1175/BAMS-D-18-0005.1>
- Harvey, T., Serduke, F., Edwards, L., & Peters, L. (1992). *KDFOC3: A nuclear fallout assessment capability* (tech. Rep.). Lawrence Livermore National Laboratory. Retrieved from <https://nrl.llnl.gov/content/mods/publications/op-model-description-evaluation/UCRL-TM-222788.pdf>
- Jaruga, A., & Pawlowska, H. (2018). Libcloudpp++ 2.0: Aqueous-phase chemistry extension of the particle-based cloud microphysics scheme. *Geoscientific Model Development*, 11(9), 3623–3645. <https://doi.org/10.5194/gmd-11-3623-2018>
- Jung, J., Fountoukis, C., Adams, P. J., & Pandis, S. N. (2010). Simulation of in situ ultrafine particle formation in the eastern United States using PMCAMx-UF. *Journal of Geophysical Research*, 115, D03203. <https://doi.org/10.1029/2009JD012313>
- Koroglu, B., Finko, M., Saggese, C., Wagnon, S., Foster, S., McGuffin, D., et al. (2022). The influence of cooling rate on condensation of iron, aluminum, and uranium oxide nanoparticles. *Journal of Aerosol Science*, 162, 105959. <https://doi.org/10.1016/j.jaerosci.2022.105959>
- Koroglu, B., Wagnon, S., Dai, Z., Crowhurst, J. C., Armstrong, M. R., Weisz, D., et al. (2018). Gas phase chemical evolution of uranium, aluminum, and iron oxides. *Scientific Reports*, 8(1), 2045–2322. <https://doi.org/10.1038/s41598-018-28674-6>
- Kou, H., Li, W., Zhang, X., Xu, N., Zhang, X., Shao, J., et al. (2019). Temperature-dependent coefficient of surface tension prediction model without arbitrary parameters. *Fluid Phase Equilibria*, 484, 53–59. <https://doi.org/10.1016/j.fluid.2018.11.024>
- McGuffin, D. L., & Lucas, D. D. (2022). Nuclear fallout super-droplet method. [Computer Software]. USDOE National Nuclear Security Administration (NNSA). <https://doi.org/10.11578/dc.20220912.1>
- McKay, M., Beckman, R., & Conover, W. (1979). Comparison of three methods for selecting values of input variables in the analysis of output from a computer code. *Technometrics*, 21(2), 239–245. <https://doi.org/10.1080/00401706.1979.10489755>
- Morris, J., Shestakov, A., Nichols, A., Isaac, B., & Knight, K. (2021). Challenges in simulating ground interacting nuclear explosions. *Countering Weapons of Mass Destruction*, 21, 128–144. <https://www.osti.gov/pages/biblio/1769128>
- Morrison, H., van Lier-Walqui, M., Fridlind, A. M., Grabowski, W. W., Harrington, J. Y., Hoose, C., et al. (2020). Confronting the challenge of modeling cloud and precipitation microphysics. *Journal of Advances in Modeling Earth Systems*, 12(8), e2019MS001689. <https://doi.org/10.1029/2019MS001689>
- Nathans, M. W., Thews, R., Holland, W. D., & Benson, P. A. (1970). Particle size distribution in clouds from nuclear airbursts. *Journal of Geophysical Research*, 75(36), 7559–7572. <https://doi.org/10.1029/JC075i036p07559>
- Palit, S. R. (1956). Thermodynamic interpretation of the Eötvös constant. *Nature*, 177(4521), 1180. <https://doi.org/10.1038/1771180a0>
- Richter, D., MacMillan, T., & Wainwright, C. (2021). A Lagrangian cloud model for the study of marine fog. *Boundary-Layer Meteorology*. <https://doi.org/10.1007/s10546-020-00595-w>

- Seifert, A., Leinonen, J., Siewert, C., & Kneifel, S. (2019). The geometry of rimed aggregate snowflakes: A modeling study. *Journal of Advances in Modeling Earth Systems*, 11(3), 712–731. <https://doi.org/10.1029/2018MS001519>
- Seinfeld, J. H., & Pandis, S. N. (2006). *Atmospheric chemistry and physics from air pollution to climate change* (2nd ed.). John Wiley & Sons.
- Semeniuk, K., & Dastoor, A. (2018). Current state of aerosol nucleation parameterizations for air-quality and climate modeling. *Atmospheric Environment*, 179, 77–106. <https://doi.org/10.1016/j.atmosenv.2018.01.039>
- Shima, S., Kusano, K., Kawano, A., Sugiyama, T., & Kawahara, S. (2009). The super-droplet method for the numerical simulation of clouds and precipitation: A particle-based and probabilistic microphysics model coupled with a non-hydrostatic model. *Quarterly Journal of the Royal Meteorological Society*, 135(642), 1307–1320. <https://doi.org/10.1002/qj.441>
- Shima, S., Sato, Y., Hashimoto, A., & Misumi, R. (2020). Predicting the morphology of ice particles in deep convection using the super-droplet method: Development and evaluation of scale-sdm 0.2.5-2.2.0, -2.2.1, and -2.2.2. *Geoscientific Model Development*, 13(9), 4107–4157. <https://doi.org/10.5194/gmd-13-4107-2020>
- Spriggs, G. D., Neuscamman, S., Nasstrom, J. S., & Knight, K. B. (2020). Fallout cloud regimes. *Countering Weapons of Mass Destruction*, 21, 103–113. Retrieved from <https://www.osti.gov/pages/biblio/1771428>
- Sreekanth, B., Anand, S., Ikkurthi, V. R., Chaudhury, P., Sapra, B. K., Mayya, Y. S., & Chaturvedi, S. (2020). Evolution of particle metrics in a buoyant aerosol cloud from explosive releases. *Aerosol Science and Technology*, 54(6), 656–667. <https://doi.org/10.1080/02786826.2020.1723788>
- Unterstrasser, S., Hoffmann, F., & Lerch, M. (2017). Collection/aggregation algorithms in Lagrangian cloud microphysical models: Rigorous evaluation in box model simulations. *Geoscientific Model Development*, 10(4), 1521–1548. <https://doi.org/10.5194/gmd-10-1521-2017>
- Unterstrasser, S., & Sölch, I. (2014). Optimisation of the simulation particle number in a Lagrangian ice microphysical model. *Geoscientific Model Development*, 7(2), 695–709. <https://doi.org/10.5194/gmd-7-695-2014>
- U.S. Department of Energy. (2015). United States nuclear tests July 1945 through September 1992 (tech. Rep.). Las Vegas, NV, United States: National nuclear security administration Nevada field office. <https://doi.org/10.2172/1351809>
- Westervelt, D. M., Pierce, J. R., Riipinen, I., Trivittayanurak, W., Hamed, A., Kulmala, M., et al. (2013). Formation and growth of nucleated particles into cloud condensation nuclei: Model–measurement comparison. *Atmospheric Chemistry and Physics*, 13(15), 7645–7663. <https://doi.org/10.5194/acp-13-7645-2013>